GEOPHYSICS, VOL. 84, NO. 6 (NOVEMBER-DECEMBER 2019); P. B375–B386, 15 FIGS., 1 TABLE.
10.1190/GEO2018-0627.1

Case History

Frequency-dependent S-wave splitting parameters analysis: A case study from azimuthal PS data, Sanhu area of the Qaidam Basin, China

Yun Wang[1], Chao Wang[1], Jianfeng Li[2], and Yuanyuan Yue[2]

ABSTRACT

The Sanhu area, which is located in the eastern Qaidam Basin in China and formed of low-amplitude anticlinal and lithologic traps, is a favorable area for biogas exploration. The fracture systems in this area are characterized in detail with the use of frequency-dependent S-wave splitting parameters, which are sensitive to the size of the fractures. The results indicate that the delay time between slow and fast S-waves decreases rapidly with increasing frequency between 5 and 30 Hz, and then it slowly decreases to a stationary value at high frequencies. Moreover, the frequency-dependent delay times suggest that fractures of different scale have different 2D density distribution. The frequency-dependent orientation of the fractures suggests that large-scale fractures, which correspond to a low-frequency band (5–11 Hz), are oriented at approximately N48°E and have small random disturbances. The mesoscale fractures that correspond to the dominant frequency band (12–36 Hz) are oriented along approximately N54°E in the northeastern region and N45°E over the remaining area. As expected, the average fracture orientation and delay time of the dominant frequency band are consistent with previous results from conventional S-wave splitting analysis in the time domain, but the frequency-dependent fracture orientation and delay time indicate finer heterogeneity and spatial anomalies. In summary, the results show the potential for accurately characterizing fracture systems using frequency-dependent S-wave splitting parameters.

INTRODUCTION

Natural fracture systems are a crucial factor for determining the potential existence of hydrocarbon reservoirs and are a key factor in controlling fluid flow, and, ultimately, determining the production of oil and gas (Qian et al., 2007, 2008). Artificial fractures are used to enhance the connectivity, permeability, and porosity of unconventional hydrocarbon reservoirs including tight gas sands and shales, and they consequently increase the production of oil and gas. The detection and characterization of fracture systems are, therefore, essential when prospecting for new hydrocarbon reservoirs or in determining a development schedule for those that already exist (Qian et al., 2012). Over the past decade, S-wave splitting analysis has been one of the most successful methods used to understand fractures (Chapman, 2003; Tang et al., 2009; Donati et al., 2016) because S-wave splitting is affected by the orientation, density (Tatham et al., 1992), and size (Ding et al., 2017) of the fractures.

Several methods have been proposed for the extraction of S-wave splitting parameters with S- or converted S-waves. Techniques such as polarization diagrams (Crampin, 1978) and rotated seismograms (Ando et al., 1980) are initially used for measuring the splitting of S-waves. Automatic measuring techniques are subsequently used to estimate the splitting attributes of the S-waves. For example, Alford rotation analysis was first proposed and used for the two-horizontal sources and two-horizontal components of shear data (Alford, 1986), after which it was used by Gaiser (1999) on 3D multicomponent data. However, the horizontal component data need to be reorganized

Manuscript received by the Editor 28 August 2018; revised manuscript received 15 April 2019; published ahead of production 30 August 2019; published online 09 October 2019.
[1]Chinese Academy of Sciences, Institute of Geochemistry, The State Key Laboratory of Ore Deposit Geochemistry, Guiyang 550081, China. E-mail: yunwang@mail.iggcas.ac.cn; srmn28@163.com.
[2]BGP INC, China National Petroleum Corporation, Zhuozhou 072750, China. E-mail: lijianfeng921@126.com; orchid.yyy@163.com.

before this method can be used. The polarity reversal method (Li, 1998), proposed for use with 3D PS-wave data, is a robust method that is based on transverse (T) component amplitude dimming and polarity reversal on azimuths parallel with or perpendicular to the fracture orientation. Other methods, including the propagator matrix method (Nicoietis et al., 1988), layer-stripping methods (Winterstein and Meadows, 1991), the dual-source cumulative technique (Zeng and Macbeth, 1993), linear-transform techniques (Li and Crampin, 1993), the crosscorrelation technique (Ando et al., 1983; Bowman and Ando, 1987; Gao and Zheng, 1995), maximizing the radial (R)/T energy ratio (Shih et al., 1989; Vinnik et al., 1989), and singular covariance matrices (Silver and Chan, 1991) have been proposed and successfully applied. Double scan methods are also often used in the analysis of converted-wave splitting through the optimization of different objective functions. Obolentseva and Gorshkalev (1986) first use an objective function to maximize the crosscorrelation of S1 and S2, Simmons (2009) uses an objective function to minimize the energy on the T component after splitting correction, and Li (2012) uses an objective function to maximize the energy on the R component after splitting correction.

These methods have successfully been applied to artificial and natural seismic data to characterize fracture orientation and density. However, these conventional methods cannot be used to estimate the size of fractures, which is essential for the characterization of reservoirs. Studies have shown that microscale cracks and macroscale fractures can contribute to S-wave splitting (Liu et al., 1993). However, we are more interested in macroscale fractures, which control the capacity for storage in a reservoir and the flow of fluids.

There are many published observations of S-wave splitting suggesting that anisotropy is frequency-dependent. Marson-Pidgeon and Savage (1997) observe a decrease in the delay time with an increase in the frequency of earthquake seismic data. From the analysis of S-wave splitting from several earthquakes that occurred in mainland China and the Pacific slab over different frequency bands, Liu et al. (2001) and Huang et al. (2011) find that the fast wave polarization direction and the delay time in S-wave splitting are dependent on the frequency band. With the studies of frequency-dependent anisotropy from a multicomponent vertical seismic profiling (VSP) at Bluebell-Altamont Field, Utah, Liu et al. (2002, 2003) find that S-wave splitting is particularly sensitive to the size of a fracture. From the analysis of a multicomponent VSP for frequency-dependent anisotropy, Liu et al. (2006) speculate that low frequencies would provide information regarding the direction of macrofractures and high frequencies would indicate the orientation of microcracks. Chapman (2003) proposes a poroelastic equivalent medium theory to model frequency-dependent anisotropy. In his theory, the size of the fractures is one of the key parameters that control frequency-dependent anisotropy. His numerical results show that, for a fixed fracture size, anisotropy weakens with increasing frequency and is sharply attenuated at some frequencies. The region in which the attenuation occurs moves from low to high frequency with a decrease in the size of a fracture. Based on Chapman's model, Al-Harrasi et al. (2011) successfully obtain the size of the fractures present in a carbonate gas field in Oman from a microseismic data set with a grid search algorithm. Thus, in the following study, we assume that low, dominant, and higher frequencies can qualitatively indicate the information of large-scale, mesoscale, and microscale fractures, respectively. To directly obtain the frequency-dependent S-wave splitting parameters from seismic data, Han and Zeng (2011) and Zhang et al. (2013) propose a new method for the extraction of splitting parameters in the frequency domain for VSP and surface multicomponent data, respectively.

In this study, we analyze the S-wave splitting in full azimuth multicomponent seismic data acquired from the Sanhu area in the Qaidam Basin of northeastern China using the frequency domain method proposed by Zhang et al. (2013). The frequency-dependent S-wave splitting parameters provided more useful information about the fractures in the Sanhu area because they are related to fracture size.

ANALYSIS METHOD

In recent years, the frequency-dependent anisotropy effect present in earthquake data has been recognized and accepted by the international community of geophysicists. The study by Chapman (2003) indicates that it is also possible to estimate the frequency-dependent anisotropy from seismic data. Zhang et al. (2013) propose an algorithm for extracting frequency-dependent S-wave splitting parameters from surface seismic data. This algorithm is adopted in our paper and is introduced schematically in the following.

First, two Cartesian coordinate systems are defined, an acquisition coordinate system with its x-axis at the R direction and a natural coordinate system with its x-axis in the direction of the fracture. To simplify the mathematics, the direction of polarization of an initial converted S-wave $S(t)$ is assumed to be along the R direction. After propagating through the anisotropic fracture media, the S-wave $S(t)$ will split into a fast wave $\mathrm{d}_f(t)$ parallel to the fracture strike and a slow wave $\mathrm{d}_s(t)$ perpendicular to the fracture strike. Based on the vector convolution model, the fast wave $\mathrm{d}_f(t)$ and slow wave $\mathrm{d}_s(t)$ in the natural coordinate system can be written as

$$\begin{bmatrix} \mathrm{d}_f(t) \\ \mathrm{d}_s(t) \end{bmatrix} = \begin{bmatrix} a_f \cos \varphi S(t-t_f) \\ -a_s \sin \varphi S(t-t_s) \end{bmatrix}, \quad (1)$$

where ϕ denotes the fracture azimuth angle counterclockwise from the R direction, t_f and t_s are the traveltimes of the fast and slow waves, respectively, and a_f and a_s represent the attenuation of the amplitudes.

After a rotational transformation from the natural coordinate system to the acquisition coordinate system, the R and T components are obtained, which can be written as

$$\begin{bmatrix} \mathrm{d}_R(t) \\ \mathrm{d}_T(t) \end{bmatrix} = \begin{bmatrix} \cos\varphi & -\sin\varphi \\ \sin\varphi & \cos\varphi \end{bmatrix} \begin{bmatrix} a_f \cos \varphi S(t-t_f) \\ -a_s \sin \varphi S(t-t_s) \end{bmatrix}, \quad (2)$$

where $\mathrm{d}_R(t))$ and $\mathrm{d}_T(t)$ represent the observed R and R components, respectively. The rotation matrix $\mathbf{R}$ (the first matrix on the right side of equation 2) is an orthogonal matrix. By multiplying both sides of equation 2 by $\mathbf{R}^{\mathrm{T}}$, we get

$$\begin{bmatrix} \mathrm{d}_R(t)\cos\varphi + \mathrm{d}_T(t)\sin\varphi \\ -\mathrm{d}_R(t)\sin\varphi + \mathrm{d}_T(t)\cos\varphi \end{bmatrix} = \begin{bmatrix} a_f \cos\varphi S(t-t_f) \\ -a_s \sin\varphi S(t-t_s) \end{bmatrix}. \quad (3)$$

Taking the Fourier transform on both sides of equation 3, we then have

$$\begin{bmatrix} \mathrm{d}_R(\omega)\cos\varphi + \mathrm{d}_T(\omega)\sin\varphi \\ -\mathrm{d}_R(\omega)\sin\varphi + \mathrm{d}_T(\omega)\cos\varphi \end{bmatrix} = \begin{bmatrix} a_f \cos\varphi S(\omega) exp(-i\omega t_f) \\ -a_s \sin\varphi S(\omega) exp(-i\omega t_s) \end{bmatrix}. \quad (4)$$

We assume that the fast and slow waves are equal in amplitude attenuation; that is, $a_f = a_s$. By dividing the upper equation by the

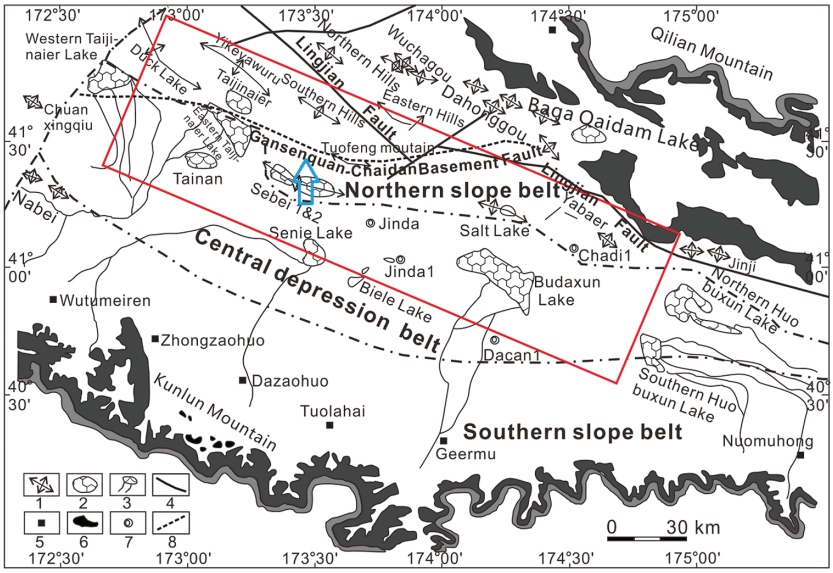

Figure 1. Geologic map of the Sanhu area in the Qaidam Basin. The blue arrow points to the area investigated in this study.

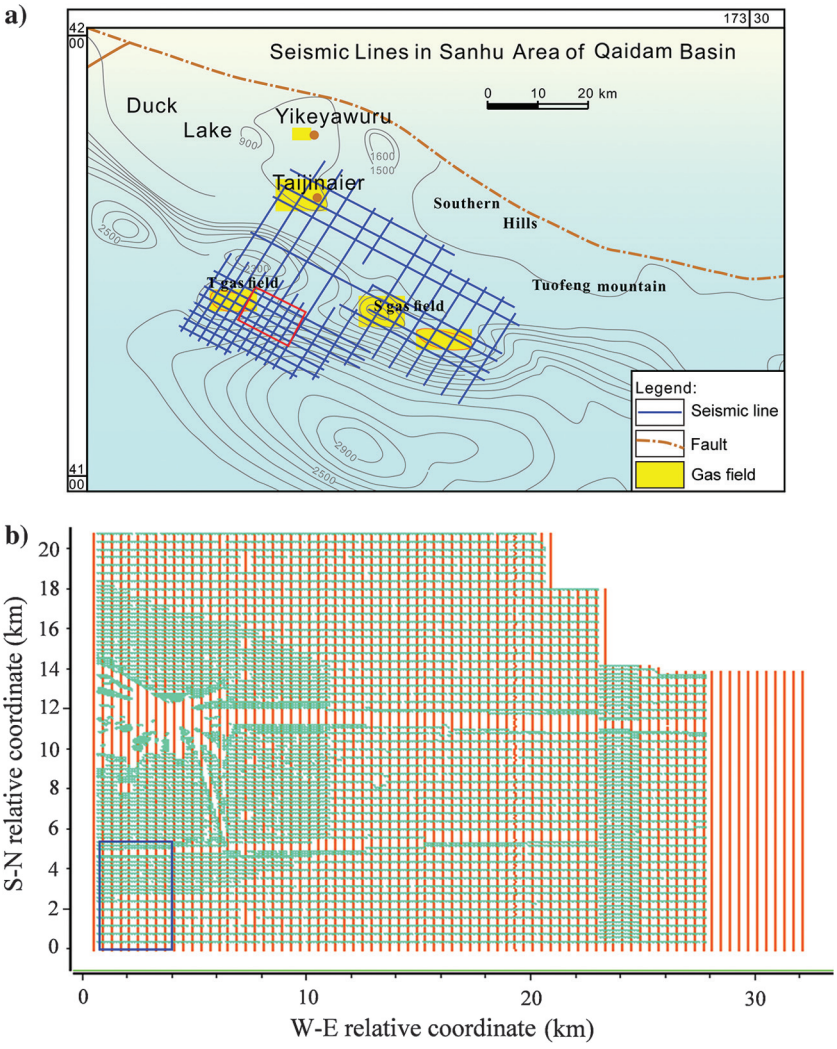

Figure 2. (a) The study area (red rectangle) and (b) seismic measurement (red represents the shot, and green represents the receiver).

lower and taking the squared norm of the two sides, we obtain the following equation:

$$\left\| \frac{\mathrm{d}_R(\omega)\cos\varphi + \mathrm{d}_T(\omega)\sin\varphi}{-\mathrm{d}_R(\omega)\sin\varphi + \mathrm{d}_T(\omega)\cos\varphi} \right\|^2 = \left\| \frac{\cos\varphi}{\sin\varphi} \right\|^2. \quad (5)$$

After simplifying equation 5, we have

$$\varphi_k = \frac{1}{2}\arctan(Q/P) + \frac{k\pi}{2},$$
$$\begin{cases} P(\omega) = \mathrm{RE}_R(\omega)\mathrm{RE}_T(\omega) + \mathrm{IM}_R(\omega)\mathrm{IM}_T(\omega), \\ Q(\omega) = \mathrm{AM}_T^2(\omega), \end{cases} \quad (6)$$

where k is any integer, RE and IM denote the real and imaginary parts of the imaginary numbers, respectively, and AM represents the amplitude. There are two solutions for ϕ in the range $0 \sim \pi$. The true value can be determined with the use of other information. By substituting the acquired fast azimuth ϕ into equation 4, we obtain the time delay of the fast and slow waves:

$$\delta t = t_s - t_f = -\frac{1}{2\pi f}\arccos\frac{-\tan\varphi(P\cos 2\varphi + W\sin 2\varphi)}{W\cos 2\varphi - P\sin 2\varphi + 0.5(\mathrm{AM}_R^2 + \mathrm{AM}_T^2)}, \quad (7)$$

where $W(f) = 1/2(\mathrm{AM}_T^2(f) - \mathrm{AM}_R^2(f))$.

Table 1. Main events in the middle and lower Quaternary formations (Q_{1+2}).

Sedimentation			Seismic events	Tectonic
Period	Epoch	Formation		
Quaternary	Q_3	Yanqiao Dabuxun Chaerhan	K_1	Neotectonics Late Himalaya
	Q_{1+2}	Seven-Spring	K_2 K_{10} T_0	
Tertiary	T_3	Shizigou	T_1	

STUDY AREA AND DATA SET

The Sanhu area is located in the eastern part of the Qaidam Basin and is presented as a red rectangle in Figure 1. Under the influence of regional compressive-torsional tectonic and strike-slip movements, the northern margin of this region is characterized by the

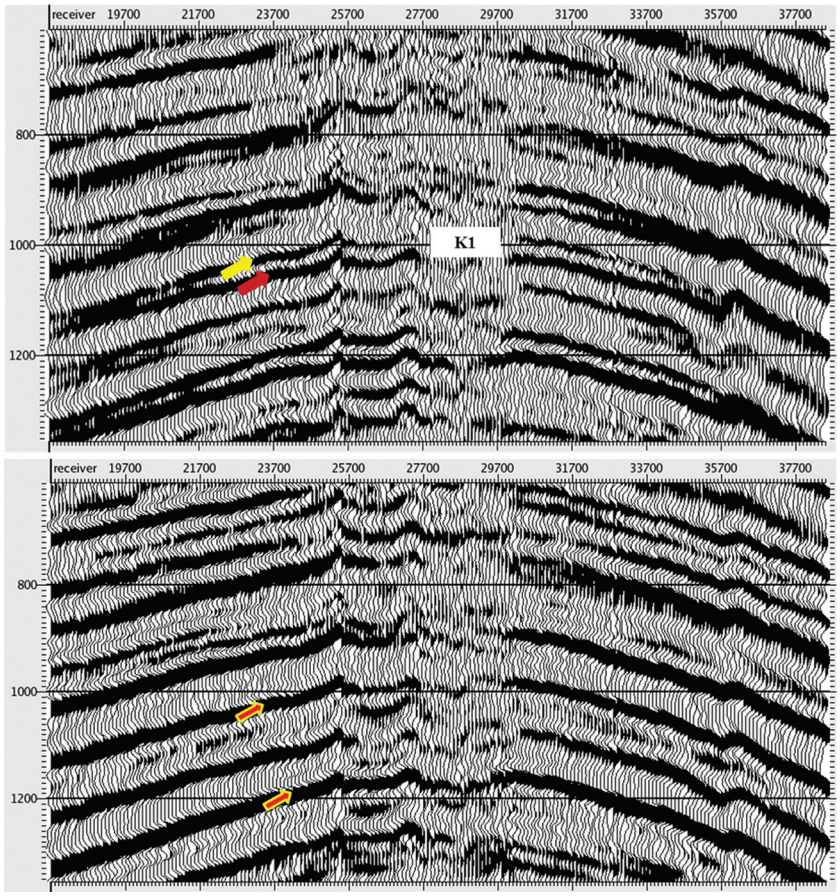

Figure 3. R component before (upper) and after (bottom) anisotropic correction with layer stripping on the K1 event.

Lingjian fault and fault-block belt, whereas the southern margin is limited by the KunBei fault system and the East Kunlun fault fold belt (Metivier et al., 1998). Three tectonic zones are therefore present in the area: the southern slope belt, the central depression zone, and the northern bend-fold zone, which are covered with thick Quaternary sedimentation, accompanied by a late Himalayan uplift. The Quaternary formations reached a thickness of more than 3000 m, with some hydrocarbon source rocks reaching up to 1600 m thick. Many potential biogas fields and areas for exploration have therefore been found in the area, in which the reservoirs and caps which are mainly distributed in the middle and deep Quaternary sedimentation, and they are mainly of continental interbedded fine sand, silts, and mudstones with strong vertical and horizontal heterogeneity (Kang et al., 2009). The shallow, Seven-Spring formations (Q_{1+2}), enriched with Quaternary biogas and with lithology mainly consisting of light-gray mudstone and silty mudstone interbedded with siltstone and fine sandstone, are the main targets for exploration (Huang, 2010).

The study area, near gas field T, which is located on the northern bend-fold slope of the Sanhu area and is represented in Figure 2a with a red rectangle, is mainly made up of low-amplitude anticlines, which are elongated toward the strike of the northwest fault (Meyer et al., 1998; Su et al., 2007). Hydrocarbons are expelled from the underlying source rocks and migrate upward along either faults or the vertical fractures of an anticline core. Oil and gas are trapped in the conventional and fracture reservoirs in the core of these anticlines (Xia et al., 2001). The low-amplitude anticlinal traps that are favorable to the accumulation of biogas (Guo et al., 2008) and are characterized as gas chimney reflections in seismic sections (Heggland, 1997; Zhang et al., 2000), are therefore the current targets for exploration, including a few lithologic traps. The prediction of fractures in these shallow anticlines and lithologic traps is of crucial importance for the characterization of gas reservoirs.

An integrated field study was performed, mainly using the 2D seismic exploration illustrated with blue lines in Figure 2a, but also including a 3D 3C seismic 2a. A digital 3C geophone with a natural frequency of 10 Hz and 3 kg of dynamite source were used with a 10 s recording length for the acquisition of the 3D 3C data. As relayed by the extent of the shot and receiver lines shown in Figure 2b, the survey area is more than 100 km^2 in total because the area with an average fold of 240 is designed as 66 km^2 and 25×25 m common depth point intervals. The interval between the source and inline was 200 m, and that between the source and receiver was 50 m, and the maximum inline and crossline offsets were 4682.55 and 2475 m, respectively. The background contours in Figure 2a represent the traveling time of the PP reflection in microseconds at the bottom of the Quaternary sedimentation.

As illustrated in Table 1, the main formations explored in the area include K2 to K10, up until event T0, where the reflection at the

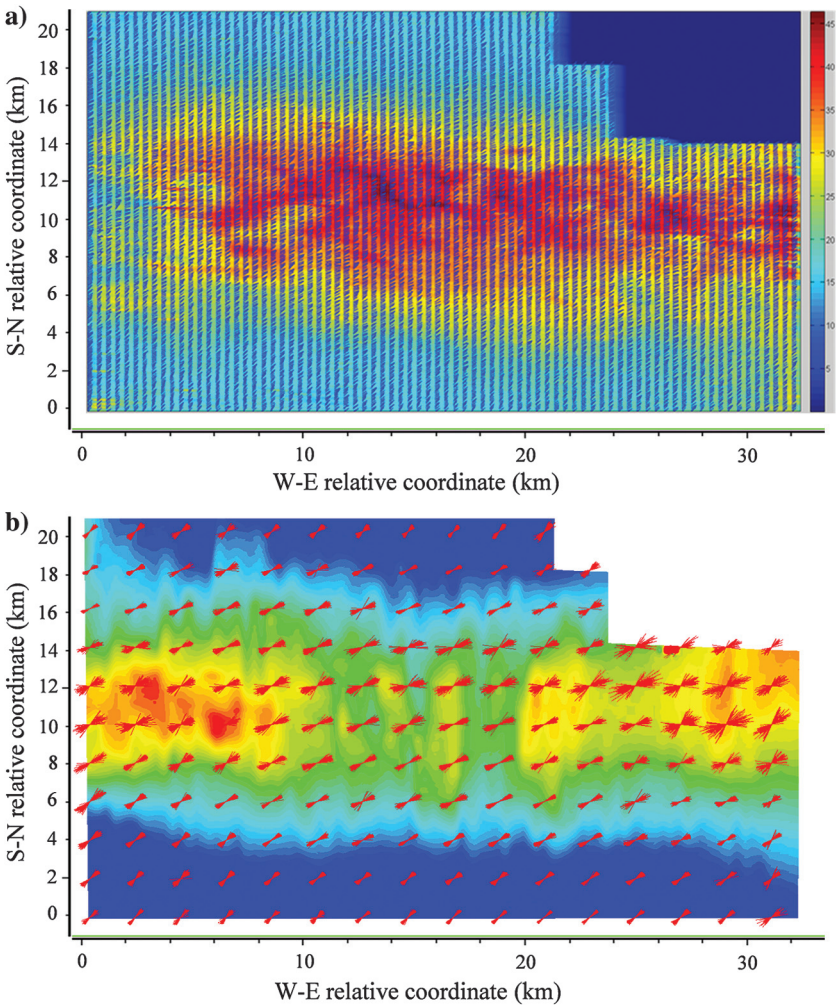

Figure 4. The distribution of fractures predicted with layer stripping on event K1 in the time domain and the color-coded time delays.

bottom of the Quaternary sedimentation and the reflection from the top interface of the Tertiary sedimentation occurs. As seen in Figure 3, when processing the PS-waves, we found that these events show an almost double-fold eye phenomenon, which may be attributed to the anisotropy in the shallow formations. Layer stripping was, therefore, carried out on the K1 event to correct for the time delays caused by S-wave splitting. The PS reflections were significantly improved after correction, as seen in Figure 3. The azimuth and density of the fractures were also calculated during this procedure, which can be found in the presentation by Yue et al. (2013) (Figure 4a). If the azimuth of the fractures is viewed in a different mode, as in Figure 4b, it is apparent that there are multidirectional fractures in the shallow formations ahead of the K1 event, which may have been caused by multiple tectonic movements in the area. A different S-wave splitting method in the frequency domain was, therefore, used for the same region to further elucidate the system of cracks.

DATA ANALYSIS AND RESULTS

The frequency-dependent anisotropic analysis method mentioned earlier was applied for the azimuth gather data set. The detailed processing steps are shown in Figure 5. Preprocessing included static correction, noise attenuation, and coordinate rotation. Full azimuth common receiver point (CRP) gathers of R and T components were then extracted from the 3D 3C seismic survey. In each full azimuth CRP gather, the traces with adjacent azimuth angles were then stacked to form a local azimuth stacked CRP gather. S-wave splitting analysis is carried out in the frequency domain, and the fast Fourier transform (FFT) is applied to the target layer data, which is picked out by a time window. The analysis consists of measuring the frequency-dependent fracture orientation and the frequency-dependent time delay between the fast and slow S-waves. For the azimuth gather, the results of the analysis are also azimuth-dependent. Therefore, we can attain a variety of results using different methods to achieve an average: frequency averaging, azimuth averaging, or frequency and azimuth averaging. For the azimuth gather, the fast wave orientation calculated with equation 6 is relative to the R direction and thus varies with the azimuth. However, the orientation of the fracture should be invariant with the azimuth. Therefore, all of the computed fast wave orientations are rotated into the R–T coordinate system of the first trace, with the R direction in the east.

In this study, the data analysis is conducted in a small area of the 3D 3C seismic survey (shown as the blue rectangle in Figure 2b). It includes 1188 full-azimuth CRP gathers, 27 inlines oriented approximately west–east and 44 crosslines oriented south–north, as seen in Figure 6. The interval between the inlines is 50 m, and the interval between the crosslines is 200 m. Each gather consists of 73 traces with an azimuth interval of 5°. The traces within a gather are sorted in a counterclockwise direction with the first source-receiver pointing toward the east. Representative R and T CPR azimuth gathers are shown in Figure 7. S-wave splitting can be observed from 400 ms to the end of the seismic record. The R component has noticeable changes in traveltime and amplitude with azimuth.

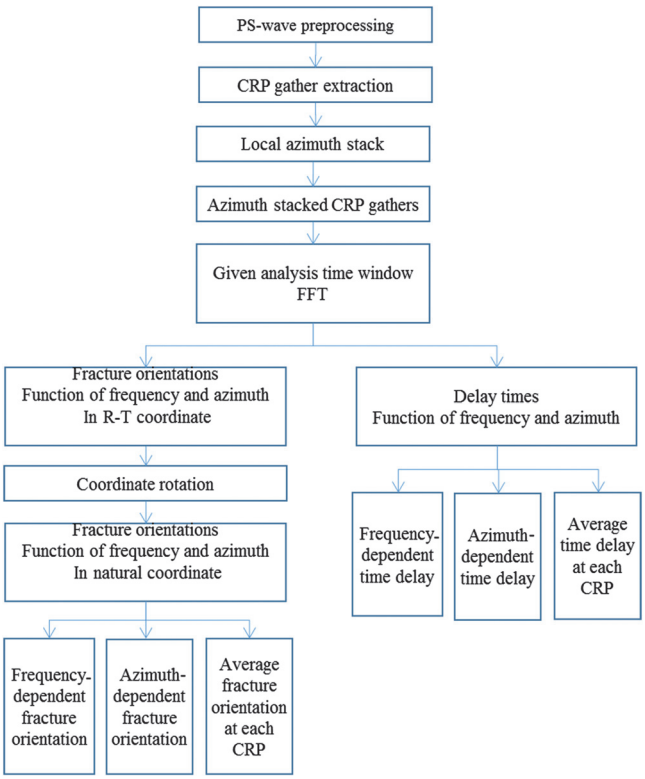

Figure 5. Procession workflow.

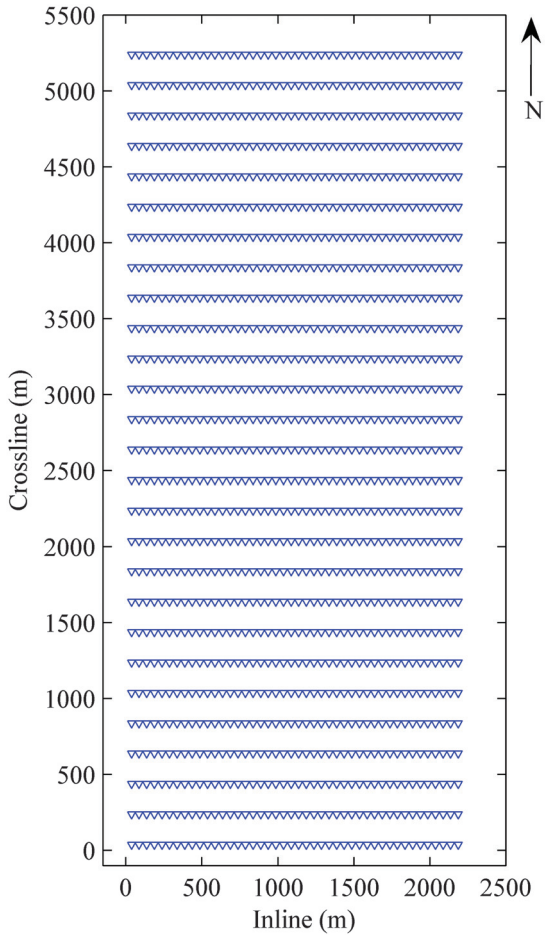

Figure 6. The basic acquisition template of 27 lines each containing 44 receiver points — a total of 1188 CRP gathers. Each inverse triangle represents a receiver point.

The T component displays polarity reversals at every 90° of azimuth. According to spectrum analysis (as shown in Figure 8), the frequency range is set to 5–50 Hz. To reduce the cumulative effects from multiple anisotropic layers, only the shallow data between 400 and 1000 ms, including the target layer, were analyzed, and the S-wave splitting was assumed to be caused by the whole of the shallow anisotropic layer.

The estimated fracture orientations are frequency- and azimuth-dependent. The fracture orientations of all azimuth traces at each

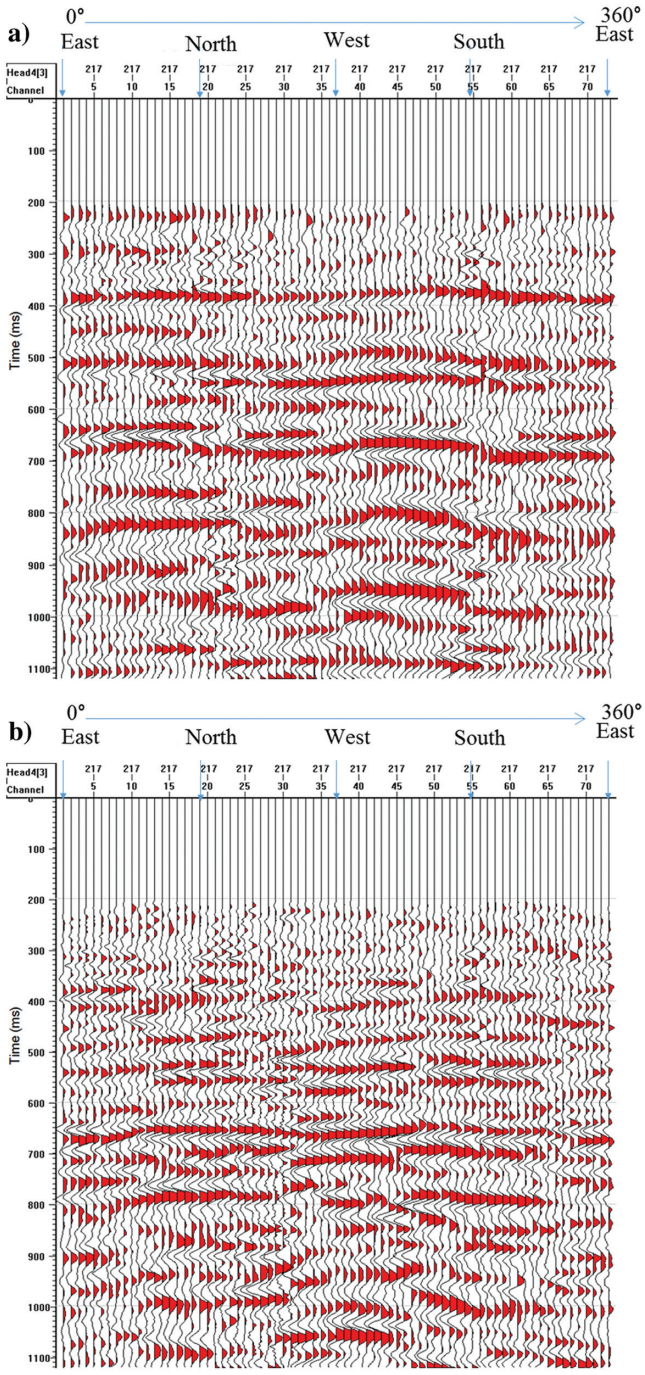

Figure 7. One CPR azimuth gather: (a) R component and (b) T component.

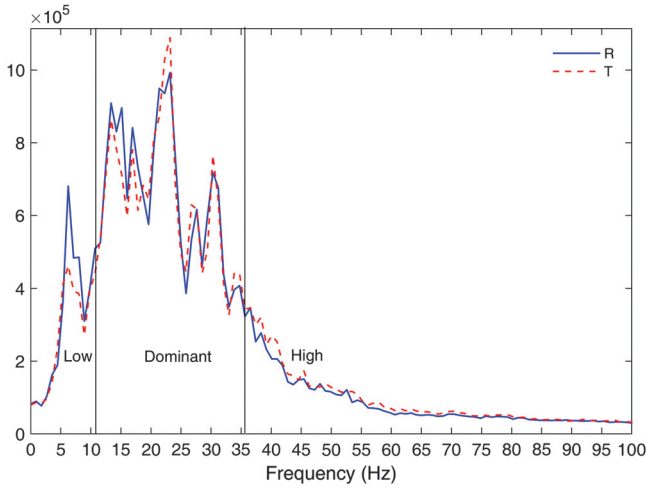

Figure 8. The averaged amplitude spectrum of one CRP gather.

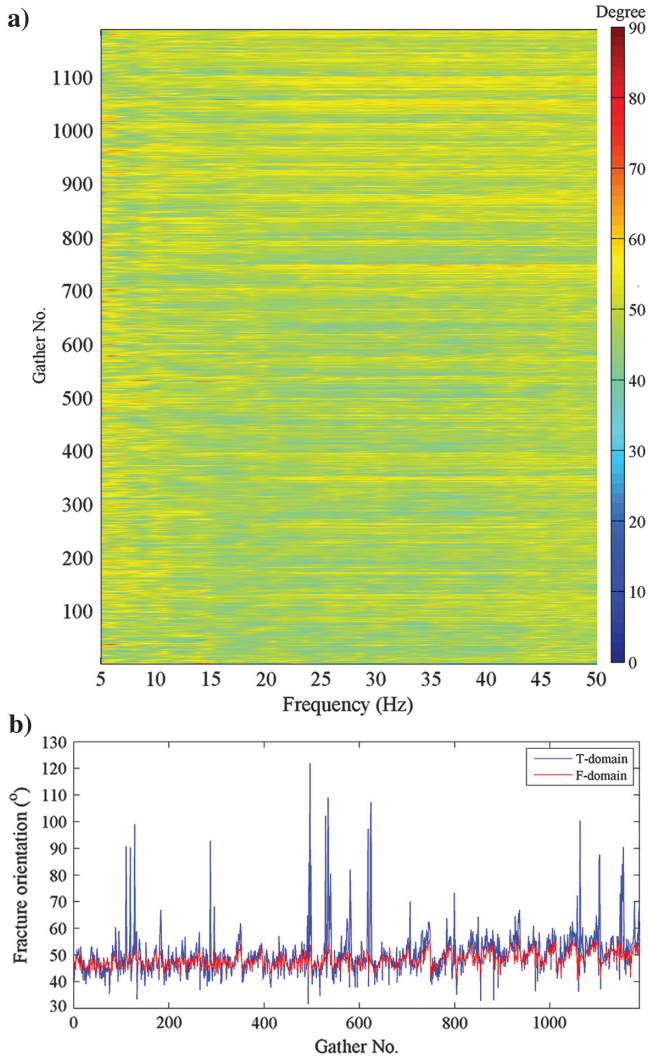

Figure 9. (a) Frequency-dependent fracture orientation and (b) comparison between fracture orientations estimated with the time-domain method (the blue line) and the frequency-domain method (the red line). The gather no. indicates the receiver-point number, which is arranged according to inline wise (as shown in Figure 6).

CRP gather were initially averaged to obtain 1188 frequency-dependent fracture orientation curves, as shown in Figure 9a. It is apparent that the fracture system is generally orientated at N45°E–N55°E in the main frequency band. The averaged fracture orientation of the main frequency band is then compared with the result calculated using the time-domain Alford rotation method, as shown in Figure 9b. The results of the two methods are consistent, but the averaged fracture orientation is smoother. The fracture orientations obtained from the time-domain method have peaks at some gather numbers, which is probably because the seismic data at these gathers are contaminated by some narrow-band noise. Narrow-band noise affects only a few frequencies in the frequency domain, and the abnormal fracture orientations computed at these frequencies can be considered as salt-and-pepper noise and is removed by median filtering. Consequently, the fracture orientation curve computed using the frequency domain method is smoother. This indicates that the estimated frequency-dependent fracture orientations are reliable. The frequency-dependent fracture orientations are also compared with those obtained via previous analysis (Yue et al., 2013). Our study area is only a part of the previous study area, located at the lower left corner. A comparison shows that the two analysis results are generally consistent with each other, but the frequency-dependent fracture orientations can provide more useful information. Figure 10 shows several fracture orientation maps at different frequencies. From the maps, we can see that the orientations of different scale fractures, corresponding to different frequency bands, show different spatial variations. At the low-frequency band, 5–10 Hz, the fracture orientation is approximately N48°E, and it has a small random disturbance over the whole study area. At the predominant frequency bands of 16–20, 21–25, and 26–30 Hz, the fracture orientation maps are clearly divided into two regions. Fractures in the northeastern region are oriented at approximately N54°E and at N45°E over the rest of the area. At the higher frequency bands of 41–45 and 46–50 Hz, the fracture orientation maps are still divided into two regions, but the azimuth difference between the two regions is smaller than that of the dominant frequency band.

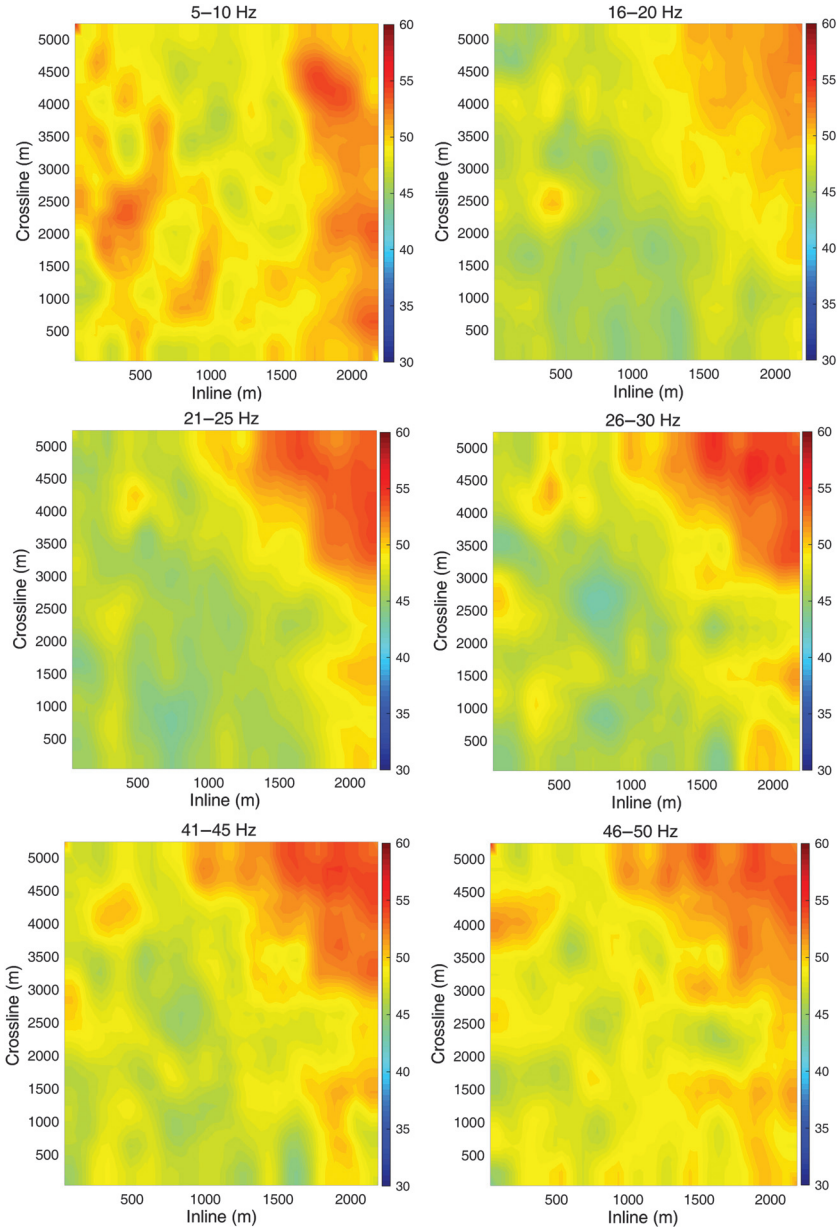

Figure 10. Maps of the fracture orientation at different frequencies.

From the above analysis, it is apparent that the fast-wave polarization is mainly at N45°–55°E over the whole Sanhu area, which is consistent with the northeast–southwest anisotropic polarization that was initiated by the India-Eurasia collision (Li et al., 2011; Zhang et al., 2012; Wang et al., 2013; Chang et al., 2017). However, the frequency-dependent polarizations provide more detailed information about the fractures in the Sanhu area. The spatial variation in the anisotropic polarization represents the heterogeneous spatial distribution of different-scale fractures. From microscale through mesoscale to macroscale fractures, which respectively relate to the higher frequency, dominant frequency, and lower frequency, there are maybe different tectonic and sedimentary factors that result in the variation in fracture distribution. The lower frequency and macroscale fractures may be controlled mainly by the low-amplitude anticline (Song and Wang, 1993).

The estimated frequency-dependent delay time reveals more significant information. The delay time is a function of azimuth and frequency. Figure 11a–11d shows the delay time as a function of azimuth at four different frequencies, 8, 12, 20, and 30 Hz. In Figure 11, the horizontal ordinate is the receiver-point number, which is arranged according to inline wise, and the blue area (except for that at 90° azimuth) indicates that no seismic data are apparent. We can see that the delay time varies with the azimuth at low frequency. Generally, the delay time is

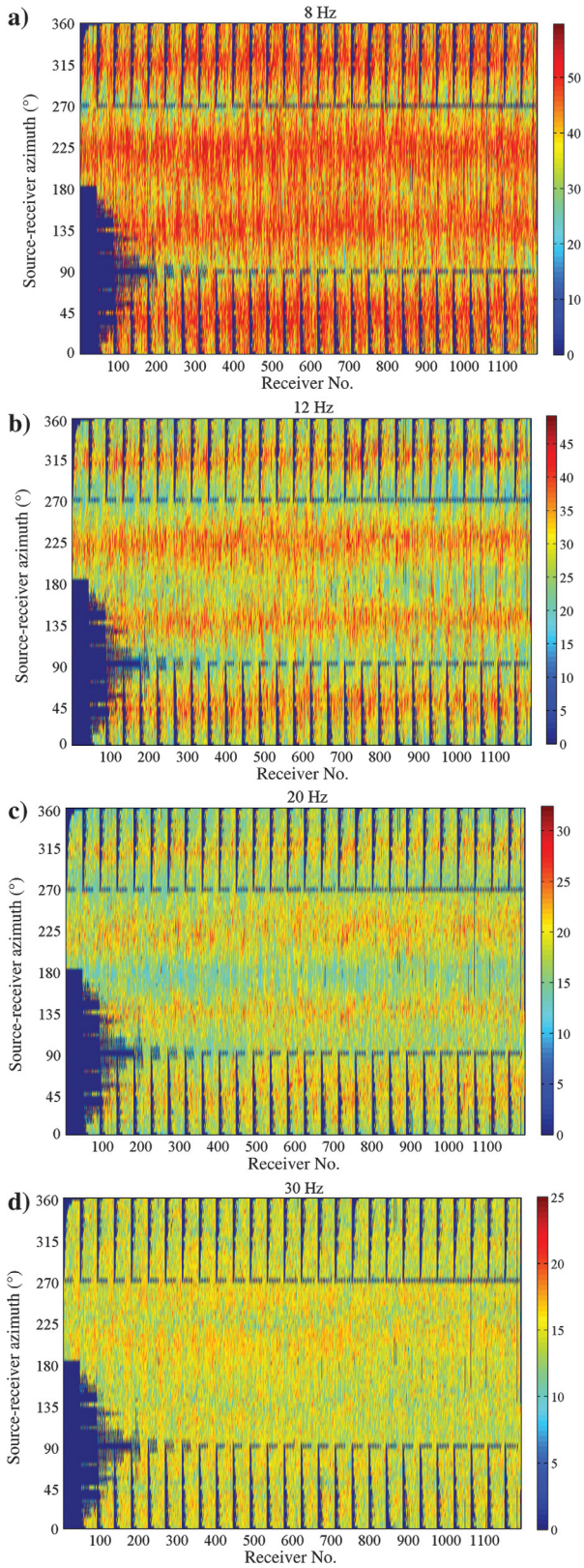

Figure 11. Delay time (unit: ms) as a function of azimuth at frequency of (a) 8 Hz, (b) 12 Hz, (c) 20 Hz, and (d) 30 Hz. The *x*-axis represents the receiver-point number, which is arranged according to inline wise (as shown in Figure 6), and the *y*-axis represents the azimuth of the 73 traces in a CRP gather, $(0 \sim 72) \times 5 = 0 \sim 360°$.

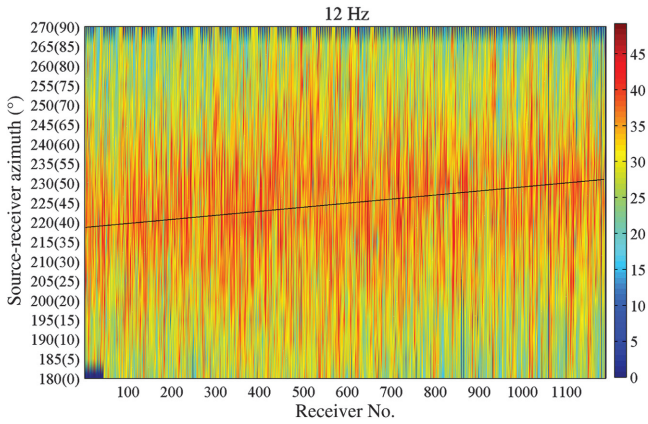

Figure 12. Delay time as a function of azimuth at 12 Hz. A magnification of part of Figure 11b.

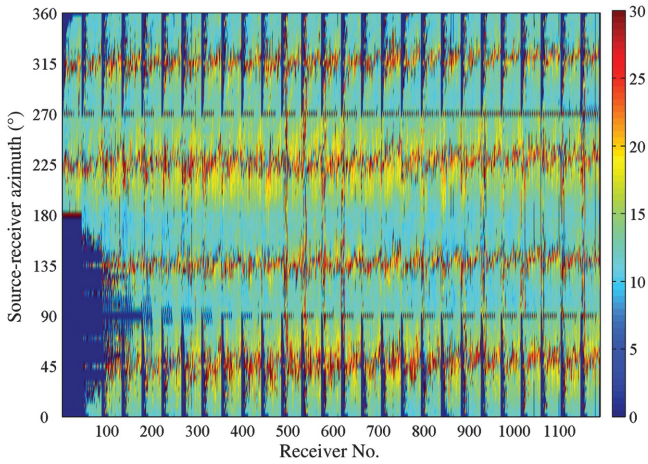

Figure 13. The delay time computed with the time-domain Alford rotation method. The *x*-axis represents the receiver-point number, which is arranged according to inline wise (as shown in Figure 6), and the *y*-axis represents the azimuth of the 73 traces in a CRP gather, $(0 \sim 72) \times 5 = 0 \sim 360°$.

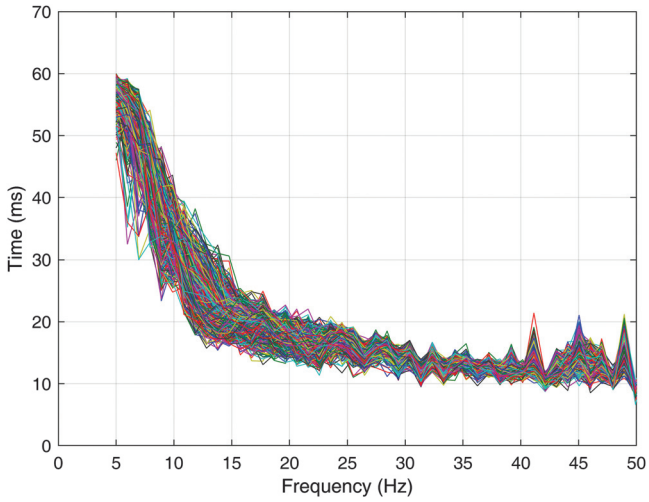

Figure 14. The frequency-dependent delay time. One curve per CRP gather, with a total of 1188 curves.

greater at an azimuth that is nearly parallel or perpendicular to the fracture orientation than it is for other azimuths. This phenomenon gradually weakens with the increase in frequency. The delay time is the same in all azimuths at high frequency. Because low frequencies may correspond to large-scale fractures, whereas high frequencies correspond to small-scale fractures, we can conclude that the large-scale fractures are arranged regularly while the small-scale fractures are arranged irregularly. Figure 12 shows a magnification of part of Figure 11b. From the azimuth-dependent delay times, we can even infer that the orientation of large-scale fractures is at approximately 50° because the delay times for all receiver points have peak values near an azimuth of 50° (50° is the same as 230° in fracture orientation). Fitting these peak points with a straight line, we can see that the fracture orientations at the receiver points with small serial numbers, which correspond to the southwestern region of the study area, are smaller than those at the receiver points with large serial numbers, corresponding to the northeastern region. This is in good agreement with Figure 10. The delay time computed with the time-domain Alford rotations method is shown in Figure 13. This suggests that the delay time also varies with the azimuth and has a larger value in azimuths that are parallel with or perpendicular to the orientation of a fracture.

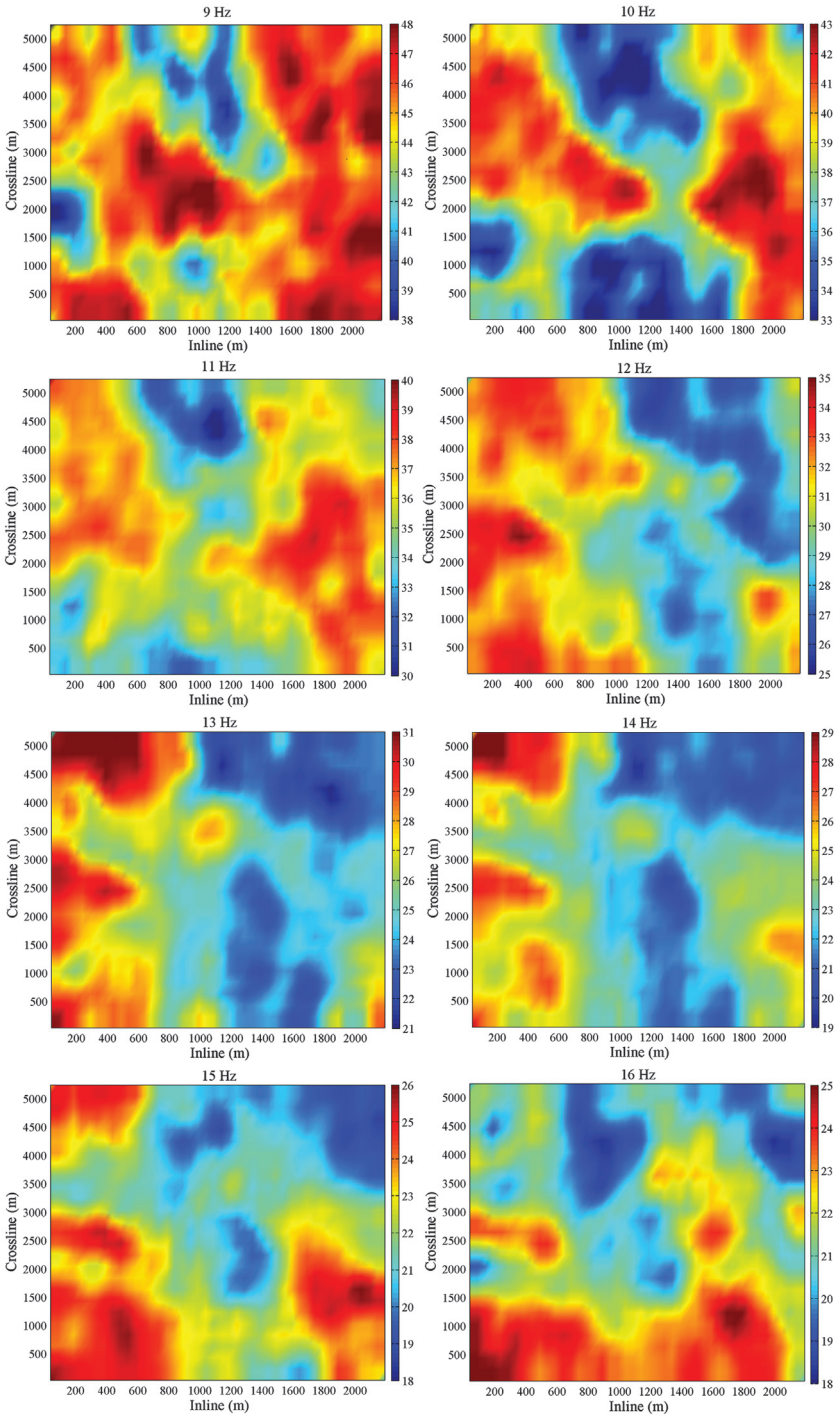

Figure 15. Maps of delay time (unit: ms) at different frequencies.

Next, the delay times of all azimuth traces at each receiver point were averaged to obtain 1188 frequency-dependent delay-time curves (as shown in Figure 14). It is apparent that the form of the relationship between the delay time and frequency is in good agreement with the numerical simulation results of Chapman (2003). The delay time is approximately 55 ms at low frequency, and it decreases rapidly with the increasing frequency between 5 and 30 Hz, and then it slowly decreases to a stationary value of approximately 12 ms at high frequencies. From the relationship between the delay time and frequency, we can infer that the predominant size of the fractures is at the meter-scale according to the numerical simulation results of Chapman (2003). The small-scale, background fractures should be relatively developed throughout the study area with a delay time of 12 ms, corresponding to the high-frequency band. Analyzing the delay time along the frequency sequence one by one, it is apparent that the delay time has obvious spatial variation. Figure 15a–15h shows the spatial variation for various frequencies from 9 up to 16 Hz. It can be seen that the delay times at 9, 10, and 11 Hz have a similar spatial variation pattern, with larger values in the east and northwest than in the southwest and northern-central region. The delay times at 12, 13, and 14 Hz have a different spatial variation pattern, with larger values in the west than in the east. When the frequency increases to 15 and 16 Hz, the red region with a longer delay time gradually moved toward the south. The delay time maps at 15 and 16 Hz are similar to the map computed with the time-domain method (Yue et al., 2013). This indicates that the fractures corresponding to these two frequencies are very developed and predominant. The time delay between the fast- and slow-splitting S-waves is mainly determined by the tectonically controlled fractures in the area. Therefore, from these frequency-dependent delay times, it is apparent that fractures of different scales have different 2D density distributions. Although the mesoscale fracture

density distribution is irregular, this can be related to the loose depositions in the shallow layer (Jin et al., 2004). To sum up, the averaged delay time on the dominant frequency band is consistent with previous results from conventional S-wave splitting analysis in the time domain (Yue et al., 2013), and the frequency-dependent time delays show more fine heterogeneity and spatial anomalies.

CONCLUSION

The frequency-dependent S-wave splitting parameters are extracted from the full-azimuth multicomponent seismic data acquired from Sanhu area in the Qaidam Basin. The averaged fracture orientation and delay time in the main frequency band are consistent with previous analysis in the time domain. This indicates that the frequency-dependent fracture orientations and delay time are reliable. It was found that the frequency-dependent splitting parameters show more detailed information about the fracture system:

1) The delay time decreases with the increasing frequency. The relationship between the delay time and frequency indicates that the predominant fracture size is on a meter scale within the gas reservoir, which should be controlled mainly by tectonics. Although the delay time at high frequencies is smaller than that at low frequencies, it still has a large value of approximately 12 ms. This indicates that the small background fractures, which may be controlled mainly by sedimentation, are relatively developed throughout the study area.
2) From the frequency-dependent delay-time maps, we know that the different-scale fractures have different 2D density distributions. The regularity of mesoscale fracture density distribution is somewhat worse, which is probably related to the loosely deposited shallow layer. The delay time maps for 15 and 16 Hz are similar to the map computed using the time-domain method; thus, the fractures corresponding to 15 and 16 Hz are very developed and predominant.
3) The large-scale fractures, corresponding to low-frequency bands, have a uniform orientation of N48°E over the whole study area. The mesoscale and large-scale fracture orientations exhibit spatial variation, which may be controlled by the low-amplitude anticline.

In conclusion, the frequency-dependent fracture orientations and delay time show potential for accurately characterizing fracture systems.

ACKNOWLEDGMENTS

Our deepest gratitude goes to the editors and reviewers, especially to H. Lynn, for their careful work and thoughtful suggestions that have helped improve this paper substantially. This research was funded by the National Natural Science Foundation of China (grant nos. 41874166, U1839208, and 41504107), the National Science and Technology Major Project (grant no. 2017ZX05018005), and the Research and Development Fund of Sinopec (grant no. P18070-5).

DATA AND MATERIALS AVAILABILITY

Data associated with this research are confidential and cannot be released.

REFERENCES

Alford, R. M., 1986, Shear data in the presence of azimuthal anisotropy: 56th Annual International Meeting, SEG, Expanded Abstracts, 476–479, doi: 10.1190/1.1893036.
Al-Harrasi, O. H., J. M. Kendall, and M. Chapman, 2011, Fracture characterization using frequency-dependent shear wave anisotropy analysis of microseismic data: Geophysical Journal International, **185**, 1059–1070, doi: 10.1111/j.1365-246X.2011.04997.x.
Ando, M., Y. Ishikawa, and H. Wada, 1980, S-wave anisotropy in the upper mantle under a volcanic area in Japan: Nature, **286**, 43–46, doi: 10.1038/286043a0.
Ando, M., Y. Ishikawa, and F. Yamazaki, 1983, Shear-wave polarization anisotropy in the upper mantle beneath Honshu, Japan: Journal of Geophysical Research, **88**, 5850–5864, doi: 10.1029/JB088iB07p05850.
Bowman, J. R., and M. Ando, 1987, Shear-wave splitting in the upper-mantle wedge above the Tonga subduction zone: Geophysical Journal of the Royal Astronomical Society, **88**, 25–41, doi: 10.1111/j.1365-246X.1987.tb01367.x.
Chang, L. J., Z. F. Ding, C. Y. Wang, and L. M. Flesch, 2017, Vertical coherence of deformation in lithosphere in the NE margin of the Tibetan plateau using GPS and shear-wave splitting data: Tectonophysics, **699**, 93–101, doi: 10.1016/j.tecto.2017.01.025.
Chapman, M., 2003, Frequency-dependent anisotropy due to meso-scale fractures in the presence of equant porosity: Geophysical Prospecting, **51**, 369–379, doi: 10.1046/j.1365-2478.2003.00384.x.
Crampin, S., 1978, Seismic-wave propagation through a cracked solid-polarization as a possible dilatancy diagnostic: Geophysical Journal of the Royal Astronomical Society, **53**, 467–496, doi: 10.1111/j.1365-246X.1978.tb03754.x.
Ding, P. B., B. R. Di, J. X. Wei, D. Wang, X. Y. Li, and Z. H. Yin, 2017, Velocity and anisotropy influenced by different scale fractures: Experiments on synthetic rocks with controlled fractures: Chinese Journal of Geophysics — Chinese Edition, **60**, 1538–1546.
Donati, M., J. L. Piazza, A. Rollet, S. Baillon, D. Marin, V. Belz, H. Toubiana, J. Castro, A. Bouheouira, and M. Raha, 2016, 3D-3C multicomponent seismic — A successful fracture characterization case study in Algeria: First Break, **34**, 35–47.
Gaiser, J. E., 1999, Applications for vector coordinate systems of converted waves obtained by multicomponent 3-D data: The Leading Edge, **18**, 1290–1300, doi: 10.1190/1.1438202.
Gao, Y., and S. H. Zheng, 1995, Cross correlation function analysis of shear wave splitting-method and example of its application: Journal of Earthquake Prediction Research, **4**, 224–237.
Guo, Z., B. Li, L. Zhang, X. Y. Li, and Y. Kong, 2008, Discussion on minimum closure for low-amplitude structural nature gas pool: A case study from Sanhu area in the Qaidam Basin: Chinese Journal of Geology, **43**, 34–49.
Han, K. F., and X. W. Zeng, 2011, Algebraic processing technique for extracting frequency-dependent shear-wave splitting parameters in an anisotropic medium: Applied Geophysics, **8**, 134–140, doi: 10.1007/s11770-011-0276-2.
Heggland, R., 1997, Detection of gas migration from a deep source by the use of exploration 3D seismic data: Marine Geology, **137**, 41–47, doi: 10.1016/S0025-3227(96)00077-1.
Huang, D. F., 2010, Cenozoic sedimentation and structure of Tainan 9 well area in Sanhu depression, Qaidam Basin: M.S. thesis, China University of Petroleum (East China).
Huang, Z. C., D. P. Zhao, and L. S. Wang, 2011, Frequency-dependent shear-wave splitting and multilayer anisotropy in Northeast Japan: Geophysical Research Letters, **38**, L08302, doi: 10.1029/2011GL046804.
Jin, Z. J., M. L. Zhang, L. J. Tang, and J. C. Li, 2004, Evolution of Meso-Cenozoic Qaidam Basin and its control on oil and gas: Oil and Gas Geology, **25**, 603–608.
Kang, N. C., G. H. Jiao, and J. M. Cai, 2009, Oil geologic feature in Sanhu depression of Qaidam Basin and next exploration and study direction: Oil Geophysical Prospecting, **44**, 508–514.
Li, X. Y., 1998, Fracture detection using P-P and P-S waves in multicomponent sea-floor data: 68th Annual International Meeting, SEG, Expanded Abstracts, 2056–2059, doi: 10.1190/1.1820357.
Li, X. Y., 2012, A stable criterion for shear wave splitting analysis: CSEG Annual Convention, Expanded Abstracts.
Li, X. Y., and S. Crampin, 1993, Linear-transform techniques for processing shear-wave anisotropy in four-component seismic data: Geophysics, **58**, 240–256, doi: 10.1190/1.1443409.
Li, Y. H., Q. J. Wu, F. G. Zhang, Q. Q. Feng, and R. Zhang, 2011, Seismic anisotropy of the northeastern Tibetan plateau for shear wave splitting analysis: Earth and Planetary Science Letters, **304**, 147–157, doi: 10.1016/j.epsl.2011.01.026.
Liu, E., S. Crampin, J. H. Queens, and W. D. Rizer, 1993, Velocity and attenuation anisotropy caused by microcracks and macrofractures in a multiazimuth reverse VSP: Canadian Journal of Exploration Geophysics, **29**, 177–188.

Liu, E., J. H. Queen, X. Y. Li, M. Chapman, H. B. Lynn, and E. M. Chesnokov, 2002, Analysis of fracture-dependent seismic anisotropy from a multicomponent VSP: 72nd Annual International Meeting, SEG, Expanded Abstracts, 101–104, doi: 10.1190/1.1816816.

Liu, E., J. H. Queen, X. Y. Li, M. Chapman, S. Maultzsch, H. B. Lynn, and E. M. Chesnokov, 2003, Observation and analysis of frequency-dependent anisotropy from a multicomponent VSP at Bluebell-Altamont Field, Utah: Journal of Applied Geophysics, **54**, 319–333, doi: 10.1016/j.jappgeo.2003.01.004.

Liu, E. R., J. H. Yue, and D. M. Pan, 2006, Frequency-dependent anisotropy: Effects of multiple fracture sets on shear-wave polarizations: Chinese Journal of Geophysics — Chinese Edition, **49**, 1401–1411, doi: 10.1002/cjg2.v49.5.

Liu, K., Z. J. Zhang, J. F. Hu, and J. W. Teng, 2001, Frequency band-dependence of S-wave splitting in china mainland and its implications: Science in China Series D: Earth Sciences, **44**, 659–665, doi: 10.1007/BF02875339.

Marson-Pidgeon, K., and M. K. Savage, 1997, Frequency-dependent anisotropy in Wellington, New Zealand: Geophysical Research Letters, **24**, 3297–3300, doi: 10.1029/97GL03274.

Metivier, F., Y. Gaudemer, P. Tapponnier, and B. Meyer, 1998, Northeastward growth of the Tibet plateau deduced from balanced reconstruction of two depositional areas: The Qaidam and Hexi corridor basins, China: Tectonics, **17**, 823–842, doi: 10.1029/98TC02764.

Meyer, B., P. Tapponnier, L. Bourjot, F. Metivier, Y. Gaudemer, G. Peltzer, G. Shunmin, and C. Zhitai, 1998, Crustal thickening in Gansu-Qinghai, lithospheric mantle subduction, and oblique, strike-slip controlled growth of the Tibet plateau: Geophysical Journal International, **135**, 1–47, doi: 10.1046/j.1365-246X.1998.00567.x.

Nicoietis, L., C. Client, and R. Lefeuvre, 1988, Shear-wave splitting measurements from multishot VSP data: 58th Annual International Meeting, SEG, Expanded Abstracts, 527–530, doi: 10.1190/1.1892327.

Obolentseva, I. R., and S. B. Gorshkalev, 1986, An algorithm for separating interfered quasi-shear waves in anisotropic media: Izv. AN SSSR. Fizika Zemli, **11**, 101–105.

Qian, Z. P., M. Chapman, and X. Y. Li, 2007, Use of multicomponent seismic data for oil-water discrimination in fractured reservoirs: The Leading Edge, **26**, 1176–1184, doi: 10.1190/1.2780789.

Qian, Z. P., X. Y. Li, and M. Chapman, 2008, Fracture characterization with azimuthal attribute analysis of PS-wave data: Modelling and application: 70th Annual International Conference and Exhibition, EAGE, Extended Abstracts, doi: 10.3997/2214-4609.20148062.

Qian, Z. P., S. H. Zhang, B. Zhao, N. Lei, and X. Y. Li, 2012, Numerical modeling of PP- and PS-wave azimuthal anisotropy in HTI media: Applied Geophysics, **9**, 429–439, doi: 10.1007/s11770-012-0355-z.

Shih, X. R., R. P. Meyer, and J. F. Schneider, 1989, An automated, analytical method to determine shear-wave splitting: Tectonophysics, **165**, 271–278, doi: 10.1016/0040-1951(89)90052-8.

Silver, P. G., and W. W. Chan, 1991, Shear-wave splitting and subcontinental mantle deformation: Journal of Geophysical Research: Solid Earth, **96**, 16429–16454, doi: 10.1029/91JB00899.

Simmons, J. L., 2009, Converted-wave splitting estimation and compensation: Geophysics, **74**, no. 1, D37–D48, doi: 10.1190/1.3036009.

Song, T., and X. Wang, 1993, Structural styles and stratigraphic patterns of syndepositional faults in a contractional setting: Examples from Quaidam Basin, Northwestern China: American Association of Petroleum Geologists Bulletin, **77**, 102–117.

Su, M., H. He, X. Wang, Z. Shi, and Z. Liu, 2007, Structural characteristics and its relationship with reservoir formation of Sanhu region of Qaidam Basin: China Petroleum Exploration, **4**, 24–27.

Tang, J. M., Y. Huang, X. R. Xu, T. John, and H. James, 2009, Application of converted-wave 3d/3-c data for fracture detectionin a deep tight-gas reservoir: The Leading Edge, **28**, 826–837, doi: 10.1190/1.3167785.

Tatham, R. H., M. D. Matthews, K. K. Sekharan, C. J. Wade, and L. M. Liro, 1992, A physical model study of shear-wave splitting and fracture intensity: Geophysics, **57**, 647–652, doi: 10.1190/1.1443278.

Vinnik, L. P., R. Kind, G. L. Kosarev, and L. I. Makeyeva, 1989, Azimuthal anisotropy in the lithosphere from observations of long-period S-waves: Geophysical Journal International, **99**, 549–559, doi: 10.1111/j.1365-246X.1989.tb02039.x.

Wang, Q., Y. Gao, Y. T. Shi, and J. Wu, 2013, Seismic anisotropy in the uppermost mantle beneath the northeastern margin of Qinghai-Tibet plateau: Evidence from shear wave splitting of SKS, PKS and SKKS: Chinese Journal of Geophysics — Chinese Edition, **56**, 892–905.

Winterstein, D. F., and M. A. Meadows, 1991, Shear-wave polarizations and subsurface stress directions at lost hills field: Geophysics, **56**, 1331–1348, doi: 10.1190/1.1443154.

Xia, W., N. Zhang, and X. Yuan, 2001, Cenozoic Qaidam Basin, China: A stronger tectonic inversed, extensional rifted basin: AAPG Bulletin, **85**, 715–736.

Yue, Y. Y., J. F. Li, Z. P. Qian, P. Y. Sun, and C. H. Cheng, 2013, Converted-wave splitting analysis and application: 75th Annual International Conference and Exhibition, EAGE, Extended Abstracts, doi: 10.3997/2214-4609.20130365.

Zeng, X. W., and C. Macbeth, 1993, Algebraic processing techniques for estimating shear-wave splitting in near-offset VSP data: Theory: Geophysical Prospecting, **41**, 1033–1066, doi: 10.1111/j.1365-2478.1993.tb00897.x.

Zhang, H., Y. Gao, Y. T. Shi, X. F. Liu, and Y. X. Wang, 2012, Tectonic stress analysis based on the crustal seismic anisotropy in the northeastern margin of Tibetan plateau: Chinese Journal of Geophysics — Chinese Edition, **55**, 95–104.

Zhang, J. L., Y. Wang, and J. Lu, 2013, A new algorithm for frequency-dependent shear-wave splitting parameters extraction: Journal of Geophysics and Engineering, **10**, 055005, doi: 10.1088/1742-2132/10/5/055005.

Zhang, W., J. Li, J. Zhong, Y. Fu, S. Chen, L. Jiang, J. Wang, and M. Li, 2000, A study on formation mechanism of gas-chimney and relationship with petroleum: Scientia Geologica Sinica, **35**, 449–455.